

ESTIMATION OF ACTIVE GUST LOAD ALLEVIATION PERFORMANCE CONSIDERING FLAP ACTUATOR LIMITATIONS

Melvin Nagy*, Elias Liebl*, Manuel Pusch*

* University of Applied Sciences Munich, Department of Mechanical Engineering, Automotive Engineering, Aerospace Engineering, Lothstraße 34, 80335 Munich, Germany

Abstract

The mitigation of gust-induced loads requires powerful actuators, which come at the expense of additional mass and cost. This creates a fundamental trade-off: while more capable actuators improve load alleviation, they also increase structural weight and system complexity. To address this challenge, this paper investigates how actuator limitations affect the achievable performance of active gust load alleviation for high-aspect-ratio wings. In order to quantify this dependency, an optimization-based method is developed to estimate the upper bound of achievable load reduction by directly optimizing control surface deflections in response to standardized gust excitations. The method is applied to an aeroelastic simulation model of the Flexop demonstrator aircraft, targeting minimization of the wing root bending moment. To reflect realistic actuator behavior, the optimization includes constraints on deflection, deflection rate, and deflection acceleration, as well as hinge moment and hinge power limitations, which in turn influence weight and cost of the actuation system. Results demonstrate that these actuator constraints strongly affect the attainable load reduction, defining critical trade-off analysis for actuator design. The findings provide valuable insights for early stage assessment of structural load reduction potential and support co-design studies of future aircraft configurations.

Keywords

Load Reduction, Actuator Design, High Aspect Ratio Wing, Co-Design

GLA Gust Load Alleviation
WRBM wing root bending moment
QP Quadratic Program
LTI Linear-Time-Invariant
HM hinge-moment
HP hinge-power
DT Direct Transcription
MPC Model Predictive Control

1. INTRODUCTION

The pursuit of sustainable aviation has intensified research into high-aspect-ratio wing configurations, as they promise improved aerodynamic efficiency and reduced fuel consumption. However, slender wings introduce new challenges due to their increased structural flexibility, which amplifies aeroelastic phenomena such as flutter and gust-induced loads [1]. Atmospheric disturbances can cause significant structural stresses, necessitating larger safety margins and heavier wing structures, which counteract the efficiency gains of high-aspect-ratio designs.

Active Gust Load Alleviation (GLA) has emerged as a promising approach to mitigate these structural loads. By exploiting fast responding control surfaces in combination with modern control algorithms, GLA strategies aim to reduce loads at critical cross sec-

tions like the wing root, thereby enabling lighter and more efficient wing designs. Several studies [2–4] have demonstrated the potential of active GLA systems to reduce gust induced loads. However, these investigations typically assume given actuator specifications, where often only a limited set of constraints is considered.

While GLA relies on capable actuators, practical systems face strict limits on deflection, deflection rate, and acceleration, as well as hinge-moment (HM) and hinge-power (HP). Such constraints directly bound the achievable load reduction and often dominate the sizing of the actuation system. At the same time, actuators add to aircraft mass, complexity, and cost. Hence, they are not only performance limiting but also design drivers that must be balanced against the potential benefits of active load alleviation. This strong interdependency between achievable GLA performance and actuator characteristics motivates a co-design perspective, where actuation is considered jointly with aerodynamics, structures, and control.

While the importance of actuator constraints is widely recognized, different control strategies have been proposed to incorporate them into the control law. Approaches include detuning of controller gains, which avoids saturation at the expense of perfor-

mance, control allocation methods that distribute virtual commands across multiple actuators while respecting individual limits [5]. Model Predictive Control (MPC) offers a predictive framework that inherently incorporates actuator constraints, but its reliance on simplified models for real-time feasibility limits applicability to flexible aircraft with complex dynamics [6–8]. At the same time, a systematic assessment of actuation system design drivers such as maximum deflection, deflection rate, acceleration, HM, and HP within a co-design framework remains limited. These actuation system design drivers not only affect weight and cost but also achievable GLA performance. This paper contributes to filling this gap by presenting an optimization-based framework that evaluates the upper bound of achievable GLA performance under various actuator constraints.

Direct Transcription (DT) [9], also known as optimal open-loop control, is an established method in numerical optimal control in which a continuous control problem is transformed into a finite-dimensional optimization problem. The system states as well as control inputs and outputs are discretized at pre-defined grid points along the time horizon, with the control inputs serving as the optimization decision variables. The underlying system dynamics are then enforced through constraints, which ensure consistency between successive time steps. In this paper, the direct transcription problem is formulated as a quadratic program, which is then efficiently solved using standard solvers [10].

The remainder of this paper is structured as follows: Section 2 details the optimization-based methodology for estimating GLA performance, with subsections on the objective function, actuator constraints, overall problem formulation, and necessary numerical adjustments for robustly solving it. Section 3 describes the modeling aspects, including the aeroelastic model of the Flexop demonstrator, the gust representation and the system representation in discrete-time. Section 4 presents and discusses the numerical results for different actuator constraint scenarios. Finally, Section 5 concludes the paper with a summary of the main findings and their implications for future co-design studies.

2. GUST LOAD ALLEVIATION PERFORMANCE ESTIMATION

To trade off GLA performance and actuator system cost/mass, a dedicated estimation framework is required for an efficient and accurate GLA performance estimation under actuation constraints. The approach developed here formulates an optimization problem that determines the upper bound of achievable load reduction while incorporating relevant actuation system design drivers as constraints.

2.1. Discrete-time System Representation

The suggested methodology for GLA performance estimation builds on discrete-time Linear-Time-Invariant (LTI) state-space representation of the considered aircraft

$$(1) \quad \begin{aligned} \mathbf{x}(k+1) &= \mathbf{A}\mathbf{x}(k) + \mathbf{B}_u\mathbf{u}(k) + \mathbf{B}_d\mathbf{d}(k) \\ \mathbf{y}(k) &= \mathbf{C}\mathbf{x}(k) + \mathbf{D}_u\mathbf{u}(k) + \mathbf{D}_d\mathbf{d}(k). \end{aligned}$$

At each discrete time step $k = 0, 1, \dots, N-1$, with time horizon N , the system is described by the input vector $\mathbf{u}(k) \in \mathbb{R}^p$, the output vector $\mathbf{y}(k) \in \mathbb{R}^q$, the disturbance vector $\mathbf{d}(k) \in \mathbb{R}^r$, and the state vector $\mathbf{x}(k) \in \mathbb{R}^m$, where p , q , and m denote the number of system inputs, outputs, and states, respectively. The matrices \mathbf{A} , $[\mathbf{B}_u \ \mathbf{B}_d]$, \mathbf{C} , and $[\mathbf{D}_u \ \mathbf{D}_d]$ are the state, input, output, and feedthrough matrix, respectively. Their dimensions are given by the length of the input, output, disturbance, and state vectors. For optimization purposes, we also consider the stacked trajectories of inputs and outputs over the finite horizon N :

$$(2) \quad \begin{aligned} \mathbf{U} &= \begin{bmatrix} \mathbf{u}(0)^\top & \mathbf{u}(1)^\top & \dots & \mathbf{u}(N-1)^\top \end{bmatrix}^\top \in \mathbb{R}^{p \cdot N}, \\ \mathbf{Y} &= \begin{bmatrix} \mathbf{y}(0)^\top & \mathbf{y}(1)^\top & \dots & \mathbf{y}(N-1)^\top \end{bmatrix}^\top \in \mathbb{R}^{q \cdot N}, \end{aligned}$$

This distinction clarifies that $\mathbf{u}(k)$ and $\mathbf{y}(k)$ represent samples at time k , while \mathbf{U} and \mathbf{Y} are the stacked trajectories over the horizon.

2.2. Objective Function

The GLA performance estimation problem is posed as an optimization task with the objective of minimizing critical structural loads. To penalize both peak and accumulated effects, these discrete-time signals are squared and weighted over the time horizon. Hence, the objective function is

$$(3) \quad J = (\mathbf{Y}_{\text{load}})^\top \mathbf{W}_1 (\mathbf{Y}_{\text{load}}),$$

where \mathbf{Y}_{load} stacks the discrete-time load signals at selected cross sections and the weighting matrix \mathbf{W}_1 is introduced to balance competing load channels.

2.3. Actuation System Design Drivers as Constraints

The following constraints are incorporated into the Quadratic Program (QP) formulation to ensure the control commands are physically realizable. In other words, actuator design drivers are implemented as constraints to be considered when evaluating the effectiveness of GLA, where linear constraints are introduced with \mathcal{C} and quadratic constraints with \mathcal{Q} .

- (\mathcal{C}_1) **Deflection Limitation**

Bounds the maximum and minimum physical deflection angles of the control surfaces. It ensures that the control inputs calculated by the optimizer do not

yield a position beyond the mechanical limits of the actuators.

- (C_2) **Deflection Rate Limitation**
Limits the maximum speed at which the ailerons can move. It originates from fundamental actuator design parameters such as available drive torque, linkage, rotor inertia, hydraulic flow capacity, and mechanical transmission characteristics. All of these parameters depend on the actuator architecture. Together, these factors define the highest achievable deflection rate. Note that while upper and lower deflection limits may differ, the deflection rate limit is generally the same in both directions. This is also the case for the deflection acceleration described next.
- (C_3) **Deflection Acceleration Limitation**
Places a bound on the acceleration of the control surfaces. While often implicitly handled by rate limits, explicitly including acceleration limits can prevent high-frequency commands. This constraint will only be implemented for physical plausibility and is not subject to further examination.
- (C_4) **Hinge Moment (HM) Limitation**
Limits the torque or moment acting at the hinge of the aileron.
- (Q_1) **Hinge Power (HP) Limitation**
Limits the power required to drive the aileron actuator. The HP is defined as the product of the HM and the deflection rate. Since the HM itself is a function of the control input, multiplying it with the deflection rate (also depending on the input) yields a term that is quadratic in the input. Therefore, this constraint naturally takes the form of a quadratic constraint.

2.4. Problem Formulation

Computing the stacked system output time series \mathbf{Y} in a recursive manner from the discrete-time model given in Section 2.1 allows formulating a QP with the control input time series \mathbf{U} as optimization variables. Combining the objective function introduced in Section 2.2 and the constraints introduced in Section 2.3 yields the QP

$$(4) \quad \begin{aligned} & \underset{\mathbf{U}}{\text{minimize}} \quad \frac{1}{2} \mathbf{U}^\top \mathbf{H} \mathbf{U} + \mathbf{f}^\top \mathbf{U} \\ & \text{subject to} \quad \mathbf{a}_i^\top \mathbf{U} \leq b_i, \quad i = 1, 2, \dots, n_i, \\ & \quad \quad \quad \mathbf{U}^\top \mathbf{Q}_j \mathbf{U} + \mathbf{q}_j^\top \mathbf{U} \leq r_j, \quad j = 1, 2, \dots, n_j \end{aligned}$$

The Hessian matrix \mathbf{H} and the linear term \mathbf{f} are derived from the objective function defined in Section 2.2 following the procedure described in the Appendix. The QP considers n_i linear constraints and n_j quadratic constraints, where the vector $\mathbf{a}_i \in \mathbb{R}^{p \cdot N}$ and matrix $\mathbf{Q}_j \in \mathbb{R}^{p \cdot N \times p \cdot N}$ are derived in a similar way to \mathbf{H} and \mathbf{f} . The objective function in Eq. 4 is convex, as its Hessian matrix \mathbf{H} is positive semi-definite. In the absence of the quadratic constraints, the formulation reduces to a convex QP, which can be efficiently solved using interior-point

methods [11]. The inclusion of the HP constraint transforms the problem into a non-convex QP. This necessitates more advanced solution techniques, for which mixed-integer programming as implemented in the Gurobi optimization toolbox [12] is employed.

2.5. Additional Aspects

In addition to the constraints listed above, residual control surface deflections must be addressed. Without further measures, the optimization may yield a new trim setting, leaving the control surfaces at a non-zero deflection even after the gust event. Hence, it must be ensured that the control surfaces should return to zero once the gust encounter has ended and oscillations have settled. To achieve this “return-to-zero” behavior without affecting GLA performance during the event itself, a sigmoid time-varying weighting is introduced. This weighting gradually increases towards the end of the time horizon, penalizing late control deflections while leaving the initial response unaffected.

The weighting factor $w(k)$ is defined as

$$(5) \quad w(k) = w_{\text{initial}} + \frac{w_{\text{final}} - w_{\text{initial}}}{1 + e^{-\beta \left(\frac{k}{N} - 0.5\right)}},$$

where w_{initial} and w_{final} are the initial and final weights, $\beta > 0$ controls the steepness of the transition.

The resulting diagonal weighting matrix is

$$(6) \quad \mathbf{W} = \text{diag}(w(0), w(1), \dots, w(N-1))$$

when considering only a single control input, otherwise the diagonal elements need to be repeated. Finally, \mathbf{W} is added to the original Hessian \mathbf{H} to obtain the weighted Hessian

$$(7) \quad \mathbf{H}_W = \mathbf{H} + \mathbf{W}.$$

Furthermore, a small regularization term $\epsilon \mathbf{I}$, with $\epsilon > 0$ a small scalar and \mathbf{I} the identity matrix, is added separately to \mathbf{H}_W to improve numerical conditioning without affecting the optimization results.

3. MODELING

3.1. Nonlinear Aeroelastic Model

The aeroelastic simulation model used in this study is based on the Flexop UAV demonstrator shown in FIG 1, a high-aspect-ratio research aircraft developed by the German Aerospace Center within the Horizon 2020 Flexop project [13]. The project pursued the improvement of aircraft efficiency and performance through aeroelastically tailored wing design combined with active control systems, enabling lighter and more flexible wings with flutter suppression and GLA. The aerodynamic loads acting on the aircraft are modeled using the Doublet Lattice Method (DLM) [14] together with a Rational Func-

tion Approximation (RFA) [15], while the structural dynamics are represented by a finite element model and subsequent modal order reduction, following the integrated modeling approach described in [16]. Detailed descriptions of the Flexop flutter demonstrator modeling are provided in [17, 18].

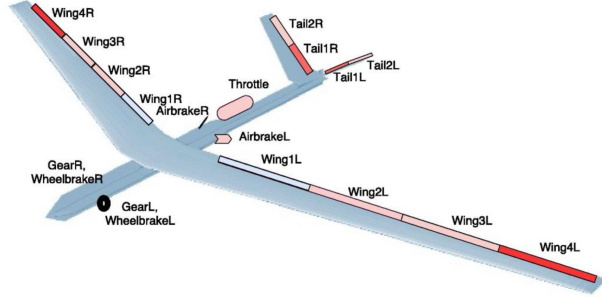


FIG 1. Flexop model and control surfaces [19]

Building on this aeroelastic simulation model, attention is given to the ailerons of the Flexop UAV, as their physical limitations directly constrain the achievable control performance. The maximum deflection is restricted to a range of $\pm 25^\circ$, while the rate of deflection is limited to $\pm 545^\circ/s$. These bounds ensure that both the magnitude and the rate of actuator motion remain within physically feasible limits. Further restrictions arise from thermal and power considerations. As detailed models of these effects are beyond the scope of this work, the constraints are introduced directly into the developed framework.

Since the provided simulation model is nonlinear, it is first linearized around a trim point. The linearized model contains 502 states, which are subsequently reduced to 40 states by applying balanced truncation. This reduction preserves the dominant input-output behavior while significantly lowering the computational complexity of the optimization. In a next step, the reduced-order model is discretized using the zero-order hold method with a sampling time of 6ms yielding the model structure given in Eq. 1.

In the present application, the input vector $\mathbf{u}(k) = [u_{\delta,4}(k) \quad d(k)]^T$ consists of the commanded deflection rate of the outer aileron pair, and the disturbance input $d(k) = d_{\text{gust}}(k)$ is the gust disturbance introduced in Section 3.2. Here, the deflection rate is selected as an input, from which the deflection and deflection acceleration are computed by using an integrator and derivative approximation (high-pass filter), respectively. All three signals together are then fed into the aeroelastic model as they contribute to the aerodynamic loads acting on the control surfaces and hence its hinge moments. Choosing the deflection rate as the actual control input allows minimizing numerical inaccuracies caused by repeated numerical differentiation or integration.

The output vector $\mathbf{y}(k) = [y_{\text{WRBM}} \quad y_{\text{HM}} \quad y_{\delta}(k) \quad \dot{y}_{\delta}(k)]^T$ is composed of all signals required for the evaluation of the objective function and the constraints. In this study, the wing root bending moment (WRBM) y_{WRBM}

and the HM y_{HM} are selected as the primary outputs of interest. Additional outputs include the aileron deflection $y_{\delta}(k)$ and deflection acceleration $\dot{y}_{\delta}(k)$, since these quantities are computed internally and are subject to actuator constraints. For HP computations, the HM $y_{\text{HM}}(k)$ is multiplied by the deflection rate $\dot{u}_{\delta,4}(k)$.

3.2. Gust Model

In this study, atmospheric disturbances are represented using a 1-cosine gust profile adapted from the European Aviation Safety Agency Certification Specification (CS-25) [20], given as:

$$d_{\text{gust}} = \frac{U_{\text{gust}}}{2} \left[1 - \cos \left(\frac{\pi V_{\text{TAS}}}{H_{\text{gust}}} \cdot t \right) \right],$$

where U_{gust} denotes the maximum gust intensity, H_{gust} the gust half-length, and V_{TAS} the true airspeed during the encounter. Following Schuhmann's approach [21], only the critical gust length is considered, assuming that this is the most critical load case.

In the aeroelastic simulation model, the gust input d_{gust} represents a symmetric gust acting at the nose of the aircraft, which is then delayed according to the flight speed to the wings and tail. To ensure consistent load distribution, all control surfaces are deflected symmetrically with respect to the aircraft's longitudinal axis.

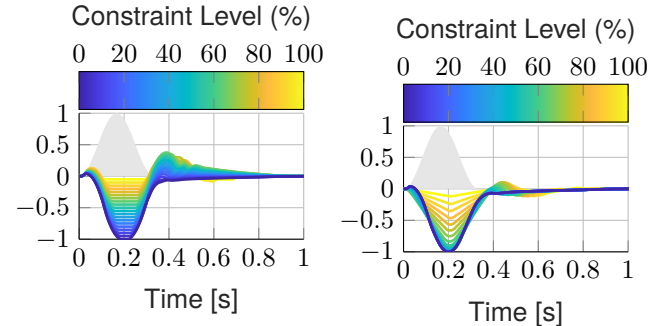
4. RESULTS AND DISCUSSION

The balance between GLA performance, expressed in terms of WRBM reduction, and the required actuator capabilities is analyzed using the performance estimation framework introduced in Section 2, applied to the Flexop demonstrator model described in Section 3. The numerical results are organized by actuator design drivers discussed in Section 2.3, with the overarching objective of minimizing the WRBM through active GLA. The following discussion highlights the impact of different actuator limitations, as outlined in Section 2.3, and compares their influence on achievable load reduction and actuator behavior.

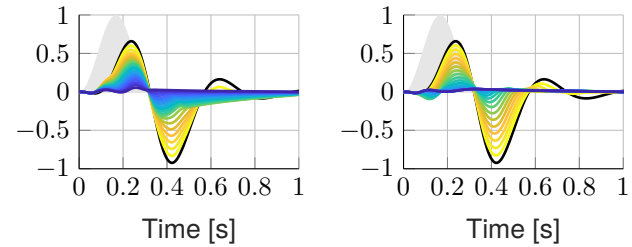
4.1. Aileron Deflection and Deflection Rate Limitation

This section investigates the influence of maximum aileron deflection and deflection rate on GLA performance. Both constraints are systematically reduced in increments of 5%, and the resulting effects on optimal aileron motion and WRBM are evaluated. The outcomes are shown in FIG 2, which compares optimized aileron deflections and the corresponding WRBM for deflection limits (left) and deflection rate limits (right). For the relative constraint level, 100% indicates a fully constrained aileron motion, whereas 0% corresponds to the nominal actuator limits introduced in Section 3. The grey-shaded area in the

background indicates the 1-cosine gust input at the nose of the aircraft. As expected, tighter limits decrease performance, where limiting aileron deflection is more performance-restricting compared to limiting deflection rate. The decay rate or settling time are similarly affected by the imposed constraints.



(a) Optimal aileron deflections with deflection limitations (b) Optimal aileron deflections with rate limitations



(c) WRBM with deflection limitations (d) WRBM with rate limitations

FIG 2. Optimal aileron deflections and GLA performance for varying deflection and deflection rate limits

In addition, Pareto fronts are generated to illustrate the attainable WRBM reduction as a function of maximum deflection and deflection rate. The results plotted in FIG 3 confirm that the achievable load reduction is strongly governed by the maximum deflection limit. It can further be seen that the influence of the deflection rate constraint becomes more pronounced as the maximum deflection increases, since at low rates the full deflection range cannot be exploited effectively.

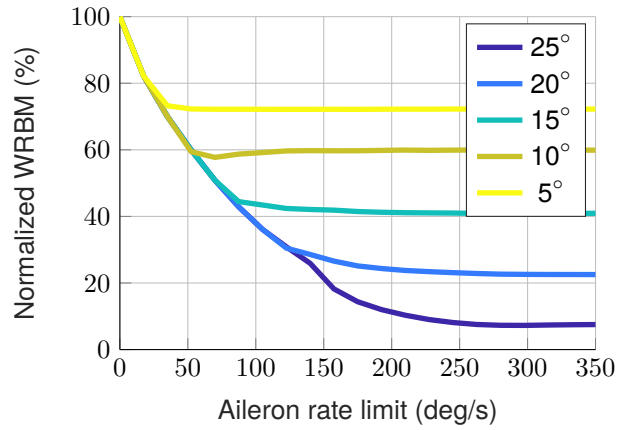
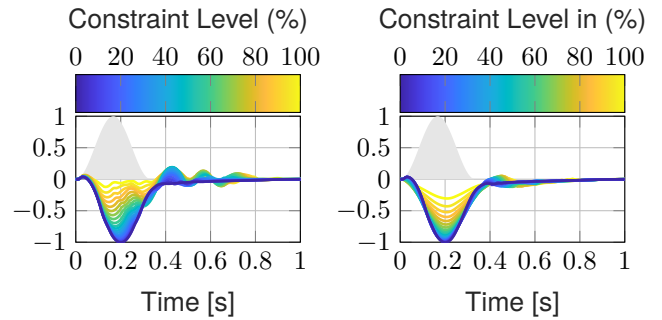


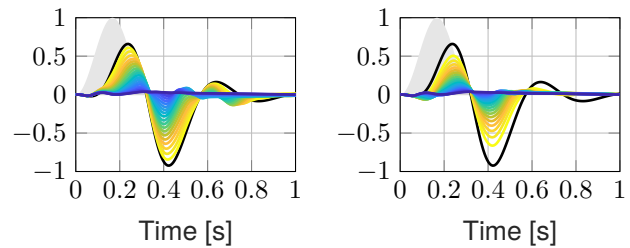
FIG 3. Pareto fronts for varying deflection limits

4.2. Hinge Moment (HM) and Hinge Power (HP) Limitation

In the second study, the allowable HM and HP are systematically reduced in increments of 5% to quantify their influence on load reduction and the required aileron deflection. The results are shown in FIG 4, where optimized aileron deflections and the corresponding WRBM for HM (left) and HP (right) are compared.



(a) Optimal aileron deflections with HM limitations (b) Optimal aileron deflections with HP limitations



(c) WRBM with HM limitations (d) WRBM with HP limitations

FIG 4. Optimal aileron deflections and GLA performance for varying hinge moment and hinge power limitations

It can be seen that a stricter HM limitation prompts a more direct and immediate control surface reaction to a gust (FIG 4a), as the actuator must instantly compensate for the aerodynamically induced moments. This behavior leads to a decaying oscillatory motion of the ailerons. In contrast, the HP constraint

regulates this effect more effectively (FIG 4b), resulting in reduced sensitivity to gusts. This improved performance arises from the inherent flexibility of the power constraint, which allows a trade-off between actuation speed and HM. As a result, the HP constraint naturally promotes a more balanced actuation strategy, which proves more effective for mitigating overall gust loads.

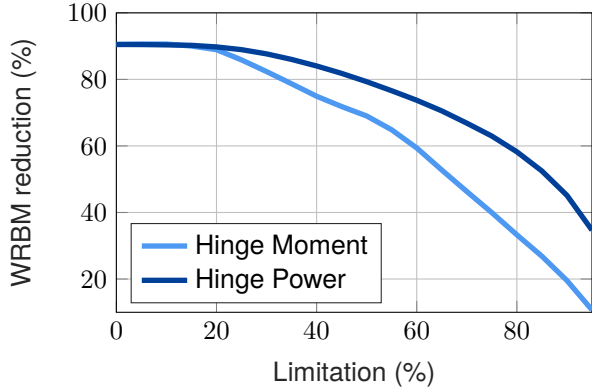


FIG 5. WRBM over time with increasing Hinge-Moment limitation

To provide a broader perspective on these trade-offs, FIG 5 presents a Pareto front comparison between HM and HP limitations. It is evident that the power constraint enables a larger overall reduction in WRBM, whereas the HM constraint leads to a faster decay of the reduction potential. For actuator design, this implies that tight HM limits impose stronger restrictions on achievable GLA than equally restrictive HP limits. From a design perspective, lower allowable HM values therefore constrain GLA performance more severely than comparable HP limits, underscoring the stronger coupling between HM capacity and load reduction potential.

5. CONCLUSION & OUTLOOK

The presented study has demonstrated that the proposed optimization-based framework enables a systematic and efficient identification of trade-offs between actuator design drivers and achievable load reduction. The underlying quadratic program formulation ensures the optimization remains computationally tractable. While only a single gust case was analyzed, the approach can readily be extended to a variety of additional load scenarios. Similarly, the study was limited to the outer aileron pair. An extension to further control surfaces would also allow the assessment of redistribution effects, which were deliberately not the focus here but could be addressed in future investigations. In this sense, the work provides valuable insights to support co-design studies of future aircraft configurations.

APPENDIX

Deriving \mathbf{H} and \mathbf{f} from discretized LTI system

The dynamics of the discrete-time LTI system are given by

$$(8) \quad \mathbf{x}(k+1) = \mathbf{A} \mathbf{x}(k) + \mathbf{B} \mathbf{u}(k),$$

$$(9) \quad \mathbf{y}(k) = \mathbf{C} \mathbf{x}(k) + \mathbf{D} \mathbf{u}(k).$$

From repeated substitution of the state equation, we obtain

$$(10) \quad \mathbf{x}(k+i) = \mathbf{A}^i \mathbf{x}(k) + \sum_{j=0}^{i-1} \mathbf{A}^{i-1-j} \mathbf{B} \mathbf{u}(k+j),$$

$$i = 1, \dots, N.$$

Stacking these relations yields the *lifted state prediction*

$$(11) \quad \mathbf{X} = \mathbf{S}_x \mathbf{x}(0) + \mathbf{S}_u \mathbf{U}, \quad \mathbf{X} \triangleq \begin{bmatrix} \mathbf{x}(k+1) \\ \mathbf{x}(k+2) \\ \vdots \\ \mathbf{x}(k+N) \end{bmatrix},$$

where

$$(12) \quad \mathbf{S}_x = \begin{bmatrix} \mathbf{A} \\ \mathbf{A}^2 \\ \vdots \\ \mathbf{A}^N \end{bmatrix}, \quad \mathbf{S}_u = \begin{bmatrix} \mathbf{B} & 0 & \dots & 0 \\ \mathbf{A}\mathbf{B} & \mathbf{B} & \dots & 0 \\ \vdots & \vdots & \ddots & \vdots \\ \mathbf{A}^{N-1}\mathbf{B} & \mathbf{A}^{N-2}\mathbf{B} & \dots & \mathbf{B} \end{bmatrix}.$$

Similarly, using $\mathbf{y}(k+i) = \mathbf{C} \mathbf{x}(k+i) + \mathbf{D} \mathbf{u}(k+i-1)$, we obtain the *lifted output prediction*

$$(13) \quad \mathbf{Y} = \mathbf{O}_x \mathbf{x}(k) + \mathbf{O}_u \mathbf{U}, \quad \mathbf{Y} \triangleq \begin{bmatrix} \mathbf{y}(k+1) \\ \mathbf{y}(k+2) \\ \vdots \\ \mathbf{y}(k+N) \end{bmatrix},$$

with

$$(14) \quad \mathbf{O}_x = \begin{bmatrix} \mathbf{C}\mathbf{A} \\ \mathbf{C}\mathbf{A}^2 \\ \vdots \\ \mathbf{C}\mathbf{A}^N \end{bmatrix}, \quad \mathbf{O}_u = \mathbf{C}\mathbf{S}_u + \mathbf{D}_{\text{bar}},$$

and \mathbf{D}_{bar} is the block-diagonal Toeplitz matrix containing \mathbf{D} on the current-input position of each output step

$$(15) \quad \mathbf{D}_{\text{bar}} = \begin{bmatrix} \mathbf{D} & 0 & \dots & 0 \\ 0 & \mathbf{D} & \dots & 0 \\ \vdots & \vdots & \ddots & \vdots \\ 0 & 0 & \dots & \mathbf{D} \end{bmatrix}.$$

The cost is formulated as

$$(16) \quad J(\mathbf{U}) = (\mathbf{Y})^\top (\mathbf{Y}), \quad \mathbf{U} \triangleq \begin{bmatrix} \mathbf{u}(k) \\ \mathbf{u}(k+1) \\ \vdots \\ \mathbf{u}(k+N-1) \end{bmatrix}.$$

Inserting eq. 13 in eq. 16 results in

$$(17) \quad \begin{aligned} J(\mathbf{U}) &= (\mathbf{O}_u \mathbf{U})^\top (\mathbf{O}_u \mathbf{U}) \\ &= \mathbf{U}^\top (\mathbf{O}_u^\top \mathbf{O}_u) \mathbf{U} + 2 \mathbf{O}_u \mathbf{U}. \end{aligned}$$

Thus the QP in the form $\min_{\mathbf{U}} \mathbf{U}^\top \mathbf{H} \mathbf{U} + \mathbf{f}^\top \mathbf{U}$ has

$$(18) \quad \mathbf{H} = \mathbf{O}_u^\top \mathbf{O}_u, \quad \mathbf{f} = 2 \mathbf{O}_u^\top (\mathbf{O}_x \mathbf{x}_k).$$

ACKNOWLEDGMENTS

The authors thank Thiemo Kier and Matthias Wüstenhagen for their support in setting up the Flexop aircraft simulation environment.

Contact address:

m.nagy0@hm.edu

References

- [1] Christopher D Regan and Christine V Jutte. Survey of applications of active control technology for gust alleviation and new challenges for lighter-weight aircraft. Technical report, 2012.
- [2] Yonghui Zhao, Chengyu Yue, and Haiyan Hu. Gust load alleviation on a large transport airplane. *Journal of Aircraft*, 53, 10 2016.
- [3] Nicolas Fezans, Hans Dieter Joos, and Christian Deiler. Gust load alleviation for a long-range aircraft with and without anticipation. *CEAS Aeronautical Journal*, 10, 2019.
- [4] Manuel Pusch, Andreas Knobloch, and Thiemo Kier. Integrated optimization of control surface layout for gust load alleviation. *CEAS Aeronautical Journal*, 10, 2019.
- [5] Manuel Pusch. Allocation of distributed flaps for gust load alleviation. In *2017 IEEE Conference on Control Technology and Applications (CCTA)*. IEEE, 2017.
- [6] H.-G. Giessler, M. Kopf, P. Varutti, T. Faulwasser, and R. Findeisen. Model predictive control for gust load alleviation. *IFAC Proceedings Volumes*, 45, 2012.
- [7] Michael Kopf, Eric Bullinger, Hans-Gerd Giessler, Stephan Adden, and Rolf Findeisen. Model predictive control for aircraft load alleviation: Opportunities and challenges. In *2018 annual american control conference (ACC)*. IEEE, 2018.
- [8] Thiemo M Kier, Martin Leitner, Özge Sülözgen, and Manuel Pusch. An integrated flexible aircraft model for optimization of lift distributions. In *AIAA Scitech 2019 Forum*, 2019.
- [9] Daniel R Herber and Athul K Sundarajan. On the uses of linear-quadratic methods in solving non-linear dynamic optimization problems with direct transcription. In *ASME International Mechanical Engineering Congress and Exposition*, volume 84546. American Society of Mechanical Engineers, 2020.
- [10] Pierre Vuillemin, David Quero Martin, and Charles Poussot-Vassal. Performance evaluation of gust load alleviation systems for flexible aircraft via optimal control. *arXiv preprint arXiv:2107.00266*, 2021.
- [11] P. E. Gill, W. Murray, M. A. Saunders, and M. H. Wright. A practical anti-cycling procedure for linearly constrained optimization. *Mathematical Programming*, 45, 1989.
- [12] Gurobi Optimization, LLC. Gurobi Optimizer Reference Manual, 2024. <https://www.gurobi.com>.
- [13] Flexop – flutter free flight envelope expansion for economical performance improvement, 2015. <https://cordis.europa.eu/project/id/636307>.
- [14] Edward Albano and William P Rodden. A doublet-lattice method for calculating lift distributions on oscillating surfaces in subsonic flows. *AIAA journal*, 7, 1969.
- [15] K. L. Roger. Airplane math modelling methods for active control design. 1977.
- [16] Thiemo Kier and Gertjan Looye. Unifying manoeuvre and gust loads analysis. 2009.
- [17] Matthias Wuestenhagen, Thiemo Kier, Yasser Meddaikar, Manuel Pusch, Daniel Ossmann, and Andreas Hermanutz. Aeroservoelastic modeling and analysis of a highly flexible flutter demonstrator. 2018.
- [18] Yasser Meddaikar, Johannes Dillinger, Thomas Klimmek, Wolf Krüger, Matthias Wuestenhagen, Thiemo Kier, Andreas Hermanutz, Mirko Hornung, Vladislav Rosov, Christian Breitsamter, James Alderman, Bela Takarics, and Bálint Vanek. Aircraft aeroservoelastic modelling of the flexop unmanned flying demonstrator. 2019.
- [19] Bálint Vanek. D4.10 Release of the flight test result and models of the a/c for the community. <https://cordis.europa.eu/project/id/636307/results>, 2019. Accessed on: June 25, 2025.
- [20] European Union Aviation Safety Agency. Certification specifications and acceptable means of compliance for large aeroplanes (cs-25), 2020. Amendment 25/20, Subpart C, §25.341.

- [21] Markus Schumann, Matthias Wuestenhagen, Manuel Pusch, and Daniel Ossmann. Model predictive gust load alleviation control for flexible aircraft. 2025.